

Parameter Trade-Offs For Imaging Spectroscopy Systems

John P. Kerekes, *Member, IEEE*, and David A. Landgrebe, *Fellow, IEEE*

Abstract—With the advent of the EOS era and configurable sensors capable of gathering ever more detailed data, users of these instruments are faced with the twin problems of specifying data acquisition parameters and extracting desired information from the voluminous data. To help better understand these problems, research has been focused on understanding the remote sensing process as a system and investigating the interrelated effects of various parameters.

An application of a system model is made to explore system parameter trade-offs for a model sensor based on HIRIS. Radiometric performance was studied, along with the effect on classification accuracy of several system parameters.

Using a model scene based on typical agricultural reflectance and atmospheric conditions, the atmosphere and sensor are seen to have significant effects on the mean received signal and noise performance. The effect of random uncorrelated errors in the radiometric calibration of the detector array is seen to degrade system performance, especially in the spectral bands below 1 μm . Accurate pixel-to-pixel relative radiometric calibration and the use of the Image Motion Compensation (IMC) option are seen to improve classification accuracy. The IMC is seen to be especially helpful under low signal-level situations such as high solar zenith angles.

The selection of feature sets based on combining spectral bands was studied under a variety of observational conditions. Feature sets chosen from characteristics of the scene performed best overall, but ones chosen based on signal-to-noise ratios were seen to be more robust.

Keywords—Remote sensing system modeling, remote sensing experiment design, HIRIS performance.

I. INTRODUCTION

AS BOTH sensor systems and processing systems become increasingly complex and configurable, the need increases for understanding the impact of various system parameters on system performance. In many remote sensing systems, the design of the sensors has been done by committee to satisfy a broad range of user communities. These committees often relied on independent trade-off studies of various components to reach an acceptable compromise in the system design. With the advent of imaging spectrometers (e.g., HIRIS [3] and MODIS [12]) with configurable observational and data selection parameters the design of the baseline system continues to need to satisfy a broad user base, but also an understanding of the impact on performance of these choices needs to be made available to help users in the design and analysis of their experiments.

Manuscript received October 25, 1989; revised February 7, 1990. This work was partially supported by the National Science Foundation through Grant ECS 8507405.

J. P. Kerekes was with the Laboratory for Applications of Remote Sensing and School of Electrical Engineering, Purdue University, West Lafayette, IN 47907. He is now with the Lincoln Laboratory, Massachusetts Institute of Technology, Lexington, MA 02173.

D. A. Landgrebe is with the Laboratory for Applications of Remote Sensing and School of Electrical Engineering, Purdue University, West Lafayette, IN 47907.

IEEE Log Number 9036048.

Recently, an approach was presented to studying these systems using simulation [6]. This approach is useful when simulated images are necessary for processing algorithm study, or when detailed spatial effects are necessary for the model. In the study of interrelated parameter effects, the variations introduced by the random number generators require many iterations of the simulation to produce reliable results. A simpler approach is one of parametric system analysis.

A parametric model for multispectral imaging systems was presented in [11]. In a recent report [7], this concept has been extended to include the entire remote sensing process through the implementation of detailed models for system components. In the system model developed in our research, we used LOWTRAN 7 [10] for the solar irradiance and atmospheric effects, as well as signal-dependent noise sources such as shot noise and relative calibration error in the sensor model.

This model has been developed with the goal being to study the radiometric performance of the system as well as to study the interrelated impact of parameters and effects on the ability of the system to discriminate among ground-cover types. Thus the primary outputs of the system model include several radiometric performance measures as well as an estimate of the obtainable classification accuracy among the ground-cover classes.

In this paper we describe an implementation of the analytical model presented in [7] (and in [9]), using a detailed model of the upcoming HIRIS instrument. We present results showing the radiometric performance of the instrument under typical conditions, as well as the results of varying several system parameters and configurations and their effect on classification accuracy. We also provide a discussion and interpretation of these results as related to the design of remote sensing experiments.

II. REMOTE SENSING SYSTEM MODELING

A. System Modeling

The remote sensing system model is based on the division of the system into three components: The scene, sensor, and processing algorithms [5]. The scene consists of all of the illumination sources, the Earth's surface, and the intervening media that contribute to the spectral radiance present at the input of the sensor. The sensor consists of all of the spectral, spatial, and radiometric effects present in converting this incident spectral radiance into digital multispectral image data. The processing consists of the operations and algorithms used in extracting the desired information from the digital image.

B. Simulation versus Analytical Modeling Approaches

In our research, two approaches to modeling the system have been implemented [7]. One is based on detailed models of the various components and is implemented as a simulation. Sim-

ulated scenes, images, and the resulting classification maps are outputs from this approach [6].

The second approach involves the use of parametric models for the various classes and analytical equations to modify the class statistics based on the various effects of system components. An estimate of the obtainable classification accuracy among the classes is the output in this approach [9].

These two approaches have their advantages and disadvantages. Table I shows a comparison between them. In the research presented in this paper we have utilized the analytical model. The following section provides a brief overview of this model.

C. Description of Analytical Model

In the analytical model, each of the various ground-cover classes in the scene are assumed to be multivariate Gaussian across the wavelength bands, and thus are completely described by their mean vector and covariance matrix. The model takes the reflectance mean and covariance statistics of each class and a description of the scene and sensor parameters and modifies these statistics by the various effects. These effects include the solar irradiance, atmospheric transmittance, additive path radiance, sensor spatial and spectral responses, electrical noise, and a calibration error model. A feature extraction process may be optionally performed through a linear transformation of the image spectral vectors.

After the statistics of each class have been modified by these functions, an estimate of the probability of error is made. Reference [13] discussed a pairwise error estimate based upon mean and covariance statistics and found it to be closely related to the actual classification error. Equation (1) shows this estimate of the probability of error P_e which uses the Bhattacharyya distance B_{kl} between classes k and l defined below, and the complementary error function as defined in (2):

$$P_e^{kl} = \text{erfc} \left\{ \sqrt{2B_{kl}} \right\} \quad (1)$$

$$\text{erfc}(\alpha) = \frac{1}{\sqrt{2\pi}} \int_{\alpha}^{\infty} e^{-(x^2/2)} dx. \quad (2)$$

The Bhattacharyya distance B_{kl} between class k and class l with mean vectors \bar{Z}_k and \bar{Z}_l and covariance matrices Σ_k and Σ_l is given as follows:

$$B_{kl} = \frac{1}{8} (Z_k - Z_l)^T \left(\frac{\Sigma_k + \Sigma_l}{2} \right)^{-1} (Z_k - Z_l) + \frac{1}{2} \log_e \frac{\left| \frac{\Sigma_k + \Sigma_l}{2} \right|}{\sqrt{|\Sigma_k| |\Sigma_l|}}. \quad (3)$$

Reference [13] also discussed an upper bound on the probability of error in the multiclass case as being the sum of the pairwise error estimates. Thus in the model the following estimate is used for the classification accuracy \hat{P}_c (in percent) among K classes:

$$\hat{P}_c = 100 \left[1 - \sum_{k=1}^K \sum_{l=1, l \neq k}^K P_e^{kl} \right]. \quad (4)$$

Since the summation of the pairwise errors is an upper bound, this estimate of the classification accuracy will be pessimistic in multiclass experiments.

TABLE I
COMPARISON BETWEEN THE SIMULATION AND ANALYTICAL APPROACHES

Simulation Model	Analytical Model
<ul style="list-style-type: none"> • Uses random vectors to represent signals and noise 	<ul style="list-style-type: none"> • Uses statistics (mean and covariance) to represent signals and noise
<ul style="list-style-type: none"> • Uses detailed sensor models based on measurements of actual instruments 	<ul style="list-style-type: none"> • Uses parametric representations of sensor components
<ul style="list-style-type: none"> • Generates synthetic scenes and images 	<ul style="list-style-type: none"> • Generates estimate of classification accuracy between ground cover classes
<ul style="list-style-type: none"> • Useful for studying these synthetic images with various processing and display methods 	<ul style="list-style-type: none"> • Useful for studying the interrelated effects of system parameters
<ul style="list-style-type: none"> • Computationally very demanding 	<ul style="list-style-type: none"> • Computationally more efficient, allowing for greater numbers of trials of different parameter choices

III. HIRIS MODEL

Model Overview

In this section a model for the High Resolution Imaging Spectrometer (HIRIS) is presented. Reference [8] contains a full description of the model. The instrument is described in [3] and is designed to be used in an on-demand mode of operation by gathering data at the request of a science investigator. Table II contains a brief overview of the instrument and its general design parameters.

The sensor has two detector arrays to cover the entire spectral response. The Visible and Near Infrared (VNIR) array covers 0.4–1.0 μm , while the Short Wave Infrared (SWIR) array covers 1.0–2.5 μm . The scene is imaged line by line as the sensor passes over. Each scene line is spectrally sampled by being dispersed across the detector arrays.

For our research the model shown in Fig. 1 is used for the HIRIS instrument. This model version has 201 equally spaced (10-nm intervals) spectral bands from 0.4 to 2.4 μm and includes most major spectral, spatial, and radiometric effects of the instrument.

Instrument parameters have been obtained from [4]. These parameter levels are based upon preliminary specifications and prototype testing. The following paragraphs and figures detail the blocks in the overall diagram and present relevant parameter values.

The spectral transmittance T_{optics} of the instrument represents the loss in signal level as a result of the transmittance through the optics. It is wavelength dependent.

The spatial response of the optics and field stop is assumed to be similar to that of the Landsat Thematic Mapper instrument, as they both have a Ground Instantaneous Field of View (GIFOV) of 30 m. In the analytical model the spatial response is assumed to have a Gaussian shape.

The radiometric conversion from the incoming spectral radiance $L_{\lambda, \text{Scene}}$ ($\text{mW}/\text{cm}^2\text{-sr-}\mu\text{m}$) is accomplished by dividing by 1000 mW/W and multiplying by the transmittance of the optics and by the $A\Omega$ (the product of the detector area and the solid angle of view) of the optics. The output of the optics model P_{λ} , the incident spectral power, is then in units of $\text{W}/\mu\text{m}$.

The incident spectral power P_{λ} at wavelength λ is converted

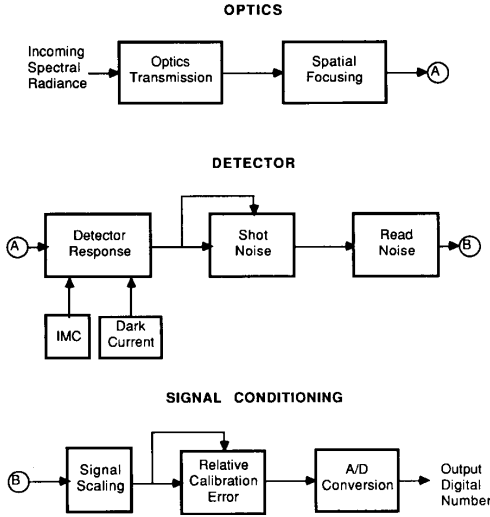


Fig. 1. HIRIS model block diagram.

TABLE II
HIRIS FUNCTIONAL PARAMETERS

Design Altitude	705 Km
Ground IFOV	30 m
Swath Width	20 Km
Spectral Coverage	0.4-2.5 μm 192 bands
Average Spectral Sample Interval	
0.4-1.0 μm	9.4 nm
1.0-2.5 μm	11.7 nm
Pointing	
Down-track	+60° / -30°
Cross-track	+20° / -20°
Data Encoding	12 b / pixel
Maximum Internal Data Rate	512 MBPS
Maximum Output Data Rate	300 MBPS
Image Motion Compensation Gain	1, 2, 4, or 8

to a number of electrons S at the detector by the integration of the incident photon level (scaled by the detector quantum efficiency η) over the pixel integration time. Thus the overall radiometric conversion from the incident spectral radiance is as follows:

$$S = L_{\lambda, \text{Scene}} \cdot \frac{1 \text{ W}}{1000 \text{ mW}} \cdot A\Omega \cdot T_{\text{optics}} \cdot \Delta\lambda \cdot \frac{1 \text{ m}}{10^6 \mu\text{m}} \cdot \frac{\lambda}{hc} \cdot \eta \cdot t. \quad (5)$$

Here $A\Omega = 1.44 \times 10^{-6} \text{ cm}^2\text{-sr}$; $\Delta\lambda = 0.01 \mu\text{m}$, the wavelength interval of spectral samples; λ = wavelength of interest (μm); $h = 6.62 \times 10^{-34} \text{ J-s}$, Planck's constant; $c = 3 \times 10^8 \text{ m/s}$, the speed of light; $t = 0.0045 \text{ s}$, pixel integration time; and η = detector quantum efficiency (function of λ).

The Image Motion Compensation (IMC) is implemented in the model by multiplying the pixel integration time by the gain state selected: 2, 4, or 8. The noise in this model consists of a deterministic dark signal level and absolute radiometric error, and random shot noise, read noise, and relative calibration error. Thermal noise has been found to be insignificant. All ran-

TABLE III
PARAMETERS OF DETECTOR ARRAYS IN TERMS OF ELECTRONS (e^-)

	VNIR	SWIR
Dark Current	$0 e^-$	$2.7 \times 10^4 e^-$
Read Noise Standard Deviation	$300 e^-$	$1000 e^-$
Full Scale Level	$5.8 \times 10^5 e^-$	$1.4 \times 10^6 e^-$

dom noise is considered to be statistically independent between noise types and spectral bands. Table III presents several parameters of the detector arrays obtained from [4].

The dark current is implemented by simply adding it to the received signal level. The absolute radiometric error is included in the detector portion of the model by multiplying the total signal by $(1 + E_R)$, where E_R is the decimal level of error. Read noise is added in as a zero-mean Gaussian random process with a standard deviation as in Table III. Within each detector array, the read noise level is assumed to be constant over wavelength.

The shot noise in the model consists of a zero-mean Gaussian random process with a standard deviation equal to the square root of the total signal level in the detectors. This total signal is comprised of the incoming radiance and the dark current level mentioned above.

The relative calibration error models the uncertainty in the radiometric calibration from pixel-to-pixel within the detector array. It is assumed to be a random process uncorrelated from pixel-to-pixel with a zero-mean uniform distribution. It is also assumed to be signal dependent; thus for a $\pm 1\%$ error the variance σ_{cal}^2 is as shown as follows:

$$\sigma_{\text{cal}}^2 = \frac{[2 \cdot 0.01 \cdot \text{signal level}]^2}{12}. \quad (6)$$

The conversion from the e^- levels of the received signal plus noise to a digital count results in a quantization error which is zero-mean and uniformly distributed with a variance as follows:

$$\sigma_{\text{quant}}^2 = \frac{1}{12} \left[\frac{\text{IMC} \cdot F}{2^Q - 1} \right]^2 \quad (7)$$

where $\text{IMC} = \text{IMC gain state}$; $F = \text{full scale electron level}$ (shown in Table III); and $Q = \text{number of radiometric bits}$ (nominally 12).

This model does not describe several effects that are present in the real HIRIS instrument. These include the non-Gaussian spatial response, the spectral dispersion, and the crosstalk between spectral bands. It is believed that these effects are of the second order and that their inclusion would not affect the results significantly.

Also, several of the parameters and graphs used here were measured during the early design phase and may change during development. These changes may affect the radiometric performance results presented here, but most probably would not significantly impact the results based on relative differences such as classification accuracy.

IV. RADIOMETRIC PERFORMANCE

A. Performance Measures

Radiometric performance of remote sensing instruments may be measured through several methods. All of these measures are a function of wavelength, atmospheric conditions, sensor

response, and sensor electrical noise. In this section, two types of measures are described and defined as they are used in our research.

Noise Equivalent Change in Reflectance ($NE\Delta\rho$) is useful in quantifying the smallest differences in the surface reflectance that are detectable by the sensor. It is defined as being the equivalent change in the reflectance of the surface to match the total noise level in the sensor. Equation (8) shows this measure for a spectral band as the quotient of the total root-mean-square sum of the noise sources and the received signal from a completely reflecting surface. Note that these parameters are dependent upon the sensor spectral band for which the calculation is being made:

$$NE\Delta\rho = \frac{\sqrt{\sigma_{\text{shot}}^2 + \sigma_{\text{read}}^2 + \sigma_{\text{quant}}^2 + \sigma_{\text{cal}}^2}}{\frac{1}{\pi} E_{\lambda, \text{Total}} T_{\lambda, \text{Atm}} B(\lambda)} \quad (8)$$

Here σ_x^2 = the variance of the sensor noise source named x ; $E_{\lambda, \text{Total}}$ = total irradiance incident upon surface; $T_{\lambda, \text{Atm}}$ = transmittance of atmosphere for path from the surface to the sensor; and $B(\lambda)$ = conversion from incident spectral radiance to number of electrons in the detector. This is the conversion shown in (5).

The Signal-to-Noise Ratio (SNR) is another measure of performance of a remote sensing instrument. It is often expressed as the log of the ratio of the signal level of interest to the total noise level. In many Earth-resource analysis remote sensing applications, the output product is some form of classification map of the observed area. The classification is usually obtained by a computer algorithm that uses the mean and covariances of the multispectral image data to distinguish between the classes. In these applications, not only are signal levels important, but so are signal power variations.

Thus in our research two types of SNR are defined. One is based on the mean signal level, while the other is computed using the covariance of the received signal. The voltage SNR is useful for determining the dynamic range required of the sensor, while the power SNR is useful for studying the sensitivity of the sensor in discriminating among surface class types.

The voltage SNR is defined for a sensor band by dividing the mean signal level by the square root of the sum of the noise levels for that band, as in the following:

$$\text{Voltage SNR} = 20 \log_{10} \left\{ \frac{\frac{1}{\pi} E_{\lambda, \text{Total}} T_{\lambda, \text{Atm}} \bar{\rho} B(\lambda)}{\sqrt{\sigma_{\text{shot}}^2 + \sigma_{\text{read}}^2 + \sigma_{\text{quant}}^2 + \sigma_{\text{cal}}^2}} \right\} \quad (9)$$

Here $\bar{\rho}$ is the mean reflectance of the surface, and $B(\lambda)$ is defined as above. The power SNR is defined for one spectral band m in the HIRIS model:

$$\text{Power SNR} = 10 \log_{10} \left\{ \frac{\sigma_m^2 \left| \frac{1}{\pi} E_{\lambda, \text{Total}} T_{\lambda, \text{Atm}} B(\lambda = m) \right|^2}{\sigma_{\text{shot}}^2 + \sigma_{\text{read}}^2 + \sigma_{\text{quant}}^2 + \sigma_{\text{cal}}^2} \right\} \quad (10)$$

Here σ_m^2 is the variance of the surface reflectance for spectral band m . Also, to include the effect of the imaging system on the power SNR, this variance must be scaled by a spatial

weighting factor $0 < W_s < 1$, as was derived in [11] and applied to our model in [9]. The results in this paper were obtained with this factor included.

In computing the voltage SNR for features derived by combining spectral bands, the total signal level is simply the sum of the individual mean signal levels, while the total noise variance is the sum of the individual noise variances. This is due to the independence assumption of the noise from spectral band to spectral band. However, in computing the power SNR for the features the signal levels cannot simply be added because of the band-to-band correlation present in the reflectance data. In this case the signal variance is the sum of the individual variances, plus terms due to the covariance σ_{mn} between each pair of wavelength bands m and n combined as follows:

$$\text{Feature Power SNR} = 10 \log_{10} \left\{ \frac{\sum_{m=1}^{M_L} \sum_{n=1}^{M_L} \sigma_{mn} B^+(\lambda = m) B^+(\lambda = n)}{\sigma_{\text{shot}}^2 + \sigma_{\text{read}}^2 + \sigma_{\text{quant}}^2 + \sigma_{\text{cal}}^2} \right\} \quad (11)$$

Here M_L is the number of wavelengths combined for the feature, while $B^+(\lambda)$ is the product of the radiance received from a completely reflecting surface and the conversion to the signal level in the sensor for the appropriate wavelength. The m, n entry in the reflectance spectral covariance matrix is denoted here as σ_{mn} . Also, the noise variances as used here are the sum of the individual wavelength variances combined appropriately for the feature.

B. Typical Radiometric Performance

In this section examples are presented of the radiometric performance of HIRIS for a typical agricultural scene. Table IV shows the details of a data set obtained from the LARS field database [1]. The reflectance data of all three classes were interpolated to 10-nm wavelength spacing and combined together, with a resulting overall mean and variation as shown in Fig. 2.

For the following examples, a baseline system configuration was defined as shown in Table V. The diffuse irradiance constant is related to the atmospheric quality and surrounding reflectance and determines the contribution of the sky or diffuse irradiance to the total downwelling irradiance.¹

Fig. 3 shows the resulting mean and variation of the digital counts produced by HIRIS for the reflectance of Fig. 2 and the system configuration of Table V. Several effects are immediately noticeable. The absorption bands of the atmosphere are present, as well as a reversal in the relative values of the amplitudes in the visible and infrared wavelengths. This reversal is due to the effects of the solar illumination and gain settings of the sensor.

The voltage and power SNR for this configuration and typical surface reflectance are shown in Fig. 4. The $NE\Delta\rho$ is shown in Fig. 5.

The voltage SNR and $NE\Delta\rho$ curves show which wavelengths have the most radiometric sensitivity. The visible and near-infrared wavelengths seem to have the best radiometric performance, at least for this typical configuration. Approximately 20% of the wavelength bands are useless for surface sensing

¹The derivation of this constant was discussed in reference [6], although it was not referred to by name. It appears there with the value 1.26 in equation (5).

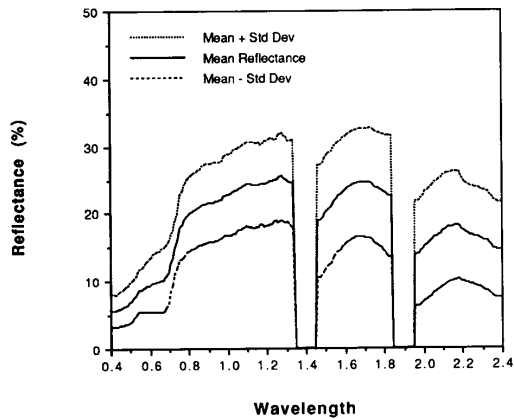


Fig. 2. Mean and variation of the surface reflectance of the Kansas winter wheat data set of Table IV.

TABLE IV
KANSAS WINTER WHEAT DATA SET

Location	Finney County, Kansas	
Date	May 3, 1977	
Spectral Classes	Number of Fields	Number of Samples
Winter Wheat	25	658
Summer Fallow	6	211
Unknown	39	682

TABLE V
RADIOMETRIC STUDY BASELINE SYSTEM CONFIGURATION

Atmospheric Model	1976 US Standard
Haze Parameter	Rural Extinction
Aerosols	Mie-Generated
Diffuse Irradiance Constant	0.84
Surface Meteorological Range	16 Km
Solar Zenith Angle	30°
Solar Azimuth Angle	180°
View Zenith Angle	0°
View Azimuth Angle	0°
Surface Albedo	0.10
IMC Gain State	1
Shot and Read Noise	Nominal
Radiometric and Calibration Error	0%
Radiometric Resolution	12 b

due to the absorption of the atmosphere. Where little or no absorption is present, the signal level is 50-100 times the noise level.

The power SNR curve has a similar shape to the voltage SNR curve, but shows a higher relative value in the visible and the longer SWIR wavelengths. This is due to the higher variation-to-mean ratio of the reflectance at these wavelengths, as can be seen in Fig. 2.

C. Effect of Relative Calibration Error on Radiometric Performance

Fig. 6 shows the effect of varying the levels of random relative calibration error on voltage SNR. The error is based upon a percentage of the received signal amplitude. Since the signal levels are highest in the visible portion of the spectrum, the

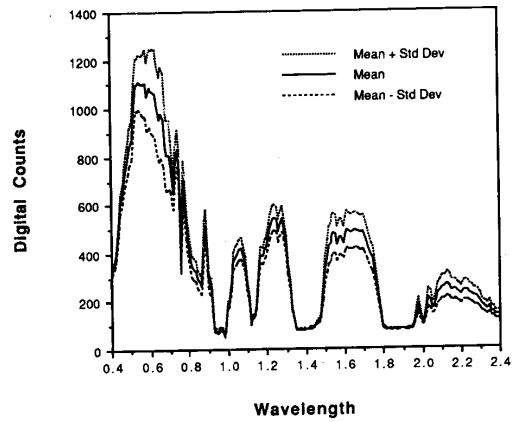


Fig. 3. Mean and variation of the image vector as received by HIRIS.

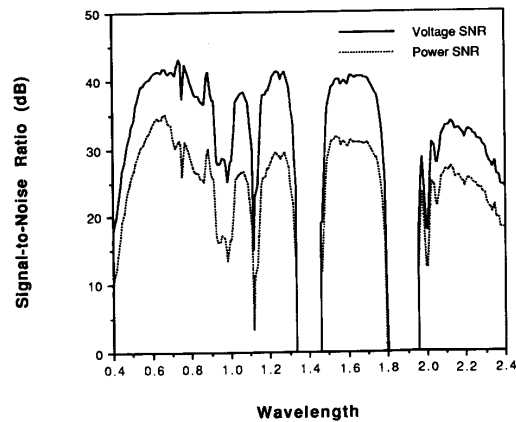


Fig. 4. Voltage and power SNR for typical reflectance.

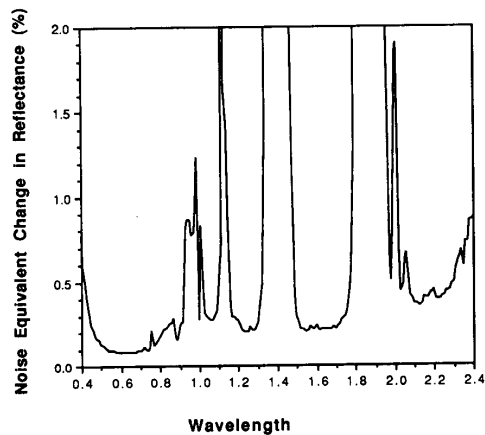


Fig. 5. $NE\Delta\rho$ for typical reflectance.

error is seen to have the greatest effect at these wavelengths. At all other wavelengths the error becomes significant at levels of 5%.

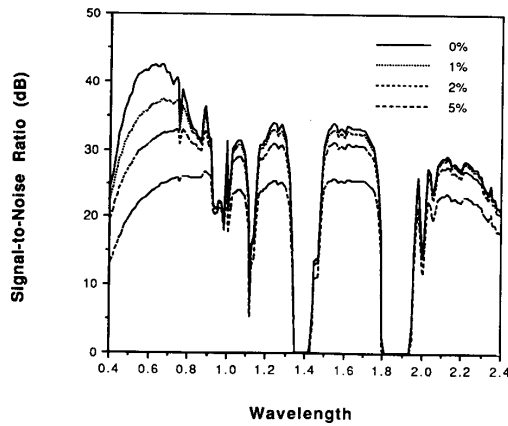


Fig. 6. Voltage SNR for various levels of relative calibration error.

These results illustrate the importance of accurately characterizing the detector array elements both before launch and during operation. Fluctuations in the response across the detector array can significantly affect the radiometric performance of the instrument.

V. CLASSIFICATION RESULTS

A. System Configuration for Experiments

Several experiments were performed to investigate the classification performance of the HIRIS sensor under different system configurations. The three classes shown in Table IV were used along with the system configuration shown in Table VI. An estimate of the classification accuracy was made using the method shown in (4).

For this work it was found to be especially useful to work with data from agricultural sites, since this type of data contains ground-cover classes which are representative of most types of ground cover and are adequately challenging, but unlike natural areas, the classes occur in large well-defined areas, thus making quantitative determination of accuracy much easier to carry out.

B. Effect of IMC and Calibration Error on Performance

Reference [7] contains the results of many experiments of varying system parameters and observing the effect on classification accuracy. The effects of IMC and relative calibration error are presented here as examples of the trends observed.

Fig. 7 shows the increase in accuracy obtained through the use of IMC. With the system configuration as shown in Table VI, the use of higher IMC states leads to higher signal levels without much increase in noise. This results in a greater separation between the classes in the feature space and higher classification accuracy.

The effect of relative calibration error is shown in Fig. 8 and is seen to be significant at errors of 1% or more. The decrease in accuracy is due to the increase in the variance of the class distributions in the feature space. This leads to more overlap between the classes and more errors in classification.

C. Effect of IMC and Solar Angle on Performance

One of the advantages of this modeling approach is the capability to study the interrelated effects of parameters. Fig. 9

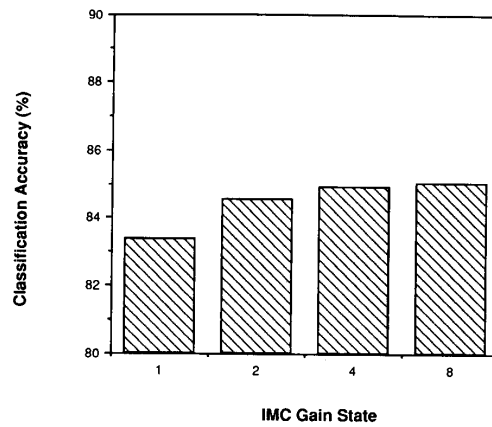


Fig. 7. Effect of IMC gain state on classification accuracy.

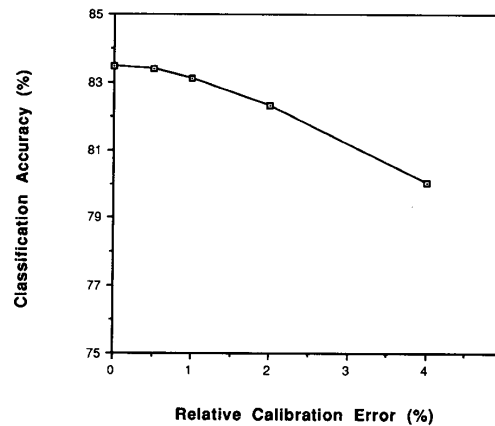


Fig. 8. Effect of relative calibration error on classification accuracy.

TABLE VI
SYSTEM CONFIGURATION FOR PARAMETER STUDIES. THE FEATURES LABELED SFD WERE DERIVED USING THE COMBINED REFLECTANCE STATISTICS OF TABLE IV AND THE SPECTRAL FEATURE DESIGN ALGORITHM DESCRIBED IN REFERENCE [2]

Scene	
Surface Meteorological Range	16 Km
Atmospheric Model	1976 US Standard
Haze Parameter	Rural Extinction
Diffuse Irradiance Constant	0.84
Solar Zenith Angle	30°
View Zenith Angle	0°
Across-Scene Spatial Correlation	0.6
Down-Scene Spatial Correlation	0.6
Sensor (HIRIS Model)	
Spatial Radius (analytical model r_0)	1.4 Scene Cells
Read Noise Level	Nominal
Shot Noise Level	Nominal
IMC Gain State	1
Relative Calibration Error	0.5%
Absolute Calibration Error	0%
Radiometric Resolution	12 b
Processing	
Feature Selection	6 SFD Features of Table VII

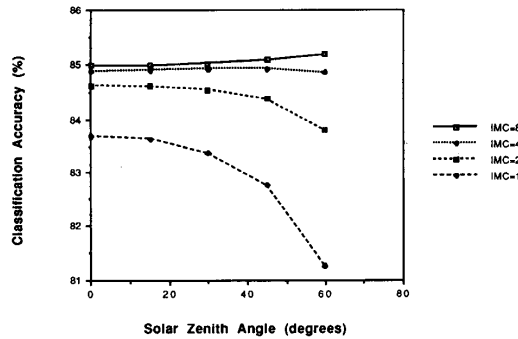


Fig. 9. Effect of IMC gain state on performance versus solar angle.

TABLE VII
WAVELENGTH BANDS (in μm) COMBINED FOR THE VARIOUS FEATURE SETS

Feature	SFD	TM	WSNR	NSNR	SSF	SSNR
1	0.52-0.66	0.45-0.52	0.40-0.70	0.51-0.56	0.59	0.54
2	0.66-0.84	0.52-0.60	0.77-0.90	0.81-0.86	0.75	0.84
3	0.70-0.92	0.63-0.69	1.00-1.10	1.02-1.07	0.81	1.04
4	1.48-1.64	0.76-0.90	1.15-1.30	1.20-1.25	1.56	1.11
5	1.98-2.20	1.45-1.75	1.50-1.74	1.59-1.64	2.10	1.61
6	2.20-2.40	2.08-2.35	1.97-2.40	2.16-2.21	2.30	2.19

The various feature sets are defined as: SFD = Spectral Feature Design Algorithm; TM = Landsat Thematic Mapper; WSNR = Wide Signal-to-Noise Ratio; NSNR = Narrow Signal-to-Noise Ratio; SSFD = Single Band Spectral Feature; and SSNR = Single Band Signal-to-Noise Ratio.

shows the effect of the IMC gain state on the relationship between solar zenith angle and classification accuracy.

In the nominal mode of $\text{IMC} = 1$, an increase in the solar zenith angle results in a decrease in the classification accuracy. However, as higher gain states are used, the effect of the solar angle diminishes, until at $\text{IMC} = 8$ when the model shows a slight increase in accuracy for high solar zenith (low elevation) angles. At these higher zenith angles the amount of solar irradiance is diminished, leading to lower signal levels as well as lower signal-dependent noise levels. These conditions allow the IMC to be most effective.

D. Feature Set Performance

Considering the voluminous amounts of data gathered by HIRIS and the fact that much of it will be either useless or redundant, it will be important to reduce this amount through feature extraction or data compression, while retaining the information content of the received data. With the fine spectral resolution and wide wavelength range of HIRIS, it will serve as an exciting source of data upon which to develop feature selection and other processing algorithms.

To investigate the effect of feature extraction on classification performance, six feature sets were chosen and evaluated. Table VII shows the wavelength bands combined to form the six features of the different feature sets.

The feature sets were chosen to give a representative selection of typical wavelengths chosen in our context of vegetative species classification. The SFD features were obtained from the algorithm presented in [2]. This algorithm uses reflectance data of the area to be observed (or similar data) to

derive features based on signal representation concepts. The TM features are included as a source of comparison to present systems. The SNR features were chosen based upon spectral regions of high SNR. These were included to investigate the relationship between classification accuracy and the combined signal-to-noise ratio. The wide, narrow, and single feature sets were chosen to investigate the effect of using progressively narrow spectral bands for the features.

Fig. 10 shows the voltage and power SNR for the various feature sets using the combined reflectance statistics of the data set in Table IV, while Fig. 11 presents the resultant classification accuracy for the baseline system of Table VI.

In this case, the SFD features performed the best for this data set, even though they did not have the highest SNR. However, since they were derived from the data used to generate the scene statistics, it is expected that they perform well. The TM feature set proved to be the next best choice, even though it was not based on the data. The wide and narrow SNR sets chosen from the gaps between absorption bands gave similar results, with very little difference in classification accuracy. The feature sets obtained by using only one wavelength band performed poorly.

An experiment was performed to compare the performance of the various feature sets over a varying scene condition. Fig. 12 shows the classification performance of the feature sets for various solar zenith angles.

From these curves it can be seen that the features derived from high SNR regions are less susceptible to changes in the scene parameters. However, overall they give less accuracy than the features obtained from the SFD algorithm. Also, the features that are obtained from only one spectral band perform poorly under all conditions.

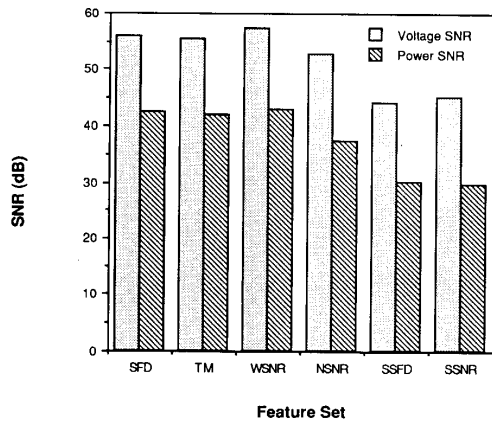


Fig. 10. Voltage and power SNR for the various feature sets of Table VII.

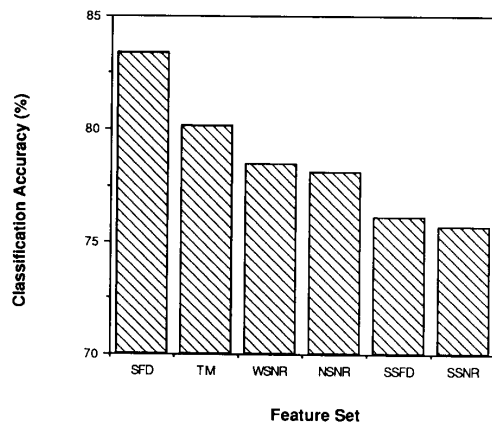


Fig. 11. Classification accuracy for the various feature sets of Table VII.

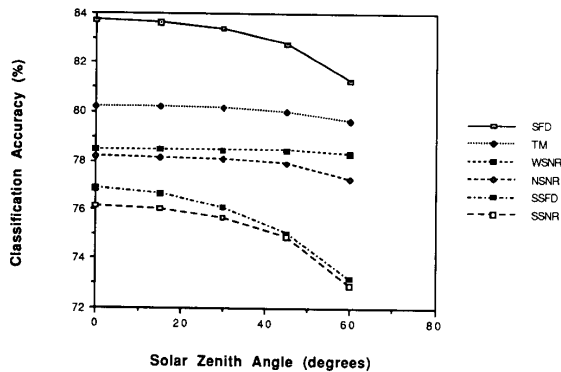


Fig. 12. Feature set performance versus solar angle.

VI. SUMMARY AND CONCLUSIONS

We have implemented a comprehensive remote sensing system model in the context of agricultural classification using a model HIRIS sensor. While this context may not be the predominant use of HIRIS, it provides an appropriate test bed to

investigate the performance of that instrument under a variety of system configurations.

We have presented results showing the radiometric performance versus spectral band for HIRIS under typical conditions. Spectral regions of high SNR were identified. The effect of a relative pixel-to-pixel calibration error was studied and seen to be most significant in the visible and very near-infrared wavelengths.

Classification performance was studied for various system configurations. Use of the IMC was seen to increase accuracy, especially under low signal-level conditions such as high solar zenith angles. Calibration error was seen to decrease accuracy.

The effectiveness of several feature set choices was investigated. Feature sets chosen from reflectance data of the observational area performed the best. However, feature sets chosen from SNR considerations were more robust in their performance over varying scene conditions.

These results are not meant to be readily applicable to all remote sensing experiments, but are rather presented as illustrative examples of observed trends and of applications of a system modeling approach.

ACKNOWLEDGMENT

The authors would like to thank L. L. Biehl of LARS for his assistance in obtaining the reflectance and image data used in these investigations. The comments and suggestions of the reviewers are also gratefully acknowledged.

REFERENCES

- [1] L. L. Biehl *et al.*, "A crops and soils data base for scene radiation research," in *Proc. 8th Int. Symp. Machine Process. of Remotely Sensed Data* (West Lafayette, IN), 1982, pp. 169-177.
- [2] C.-C. Chen and D. A. Landgrebe, "A spectral feature design system for the HIRIS/MODIS era," *IEEE Trans. Geosci. Remote Sensing*, vol. 27, pp. 681-686, Nov. 1989.
- [3] A. F. H. Goetz and M. Herring, "The high resolution imaging spectrometer (HIRIS) for Eos," *IEEE Trans. Geosci. Remote Sensing*, vol. 27, pp. 136-144, Mar. 1989.
- [4] "High-resolution imaging spectrometer (HIRIS): Phase A final report," Jet Propulsion Lab., California Instit. Technol., Pasadena, CA, Rep. JPL D-4782, Nov. 1987. (Data was also obtained from viewgraphs used in a presentation by V. Wright of JPL on Oct. 6, 1987 to the Imaging Spectrometer Science Advisory Group (ISSAG)).
- [5] J. P. Kerekes and D. A. Landgrebe, "A noise taxonomy for remote sensing systems," in *Proc. IGARSS '87* (Ann Arbor, MI), 18-21 May 1987, pp. 903-908.
- [6] ——— and ———, "Simulation of optical remote sensing systems," *IEEE Trans. Geosci. Remote Sensing*, vol. 27, pp. 762-771, Nov. 1989.
- [7] ———, "Modeling, simulation, and analysis of optical remote sensing systems," Ph.D. thesis, TR-EE 89-49, School Elec. Eng., Purdue Univ., West Lafayette, IN, Aug. 1989.
- [8] ———, "HIRIS performance study," School Elec. Eng., Purdue Univ., West Lafayette, IN, TR-EE 89-23, Apr. 1989.
- [9] ———, "An analytical model of earth observational remote sensing systems," *IEEE Trans. Syst., Man, Cybern.*, to be published.
- [10] F. X. Kneizys *et al.*, "User's guide to LOWTRAN 7," Air Force Geophys. Lab., Bedford, MA, Tech. Rep. AFGL-TR-88-0177, Aug. 1988.
- [11] B. G. Mobasser, C. D. McGillem, and P. E. Anuta, "Parametric multiclass bayes error estimator for multispectral scanner spatial model performance evaluation," Lab. Appl. Remote Sensing, Purdue Univ., West Lafayette, IN, LARS Tech. Rep. 061578, June 1978.
- [12] V. V. Salomonson, W. L. Barnes, P. W. Maymon, H. E. Montgomery, and H. Ostrow, "MODIS: Advanced facility instrument

for studies of the earth as a system," *IEEE Trans. Geosci. Remote Sensing*, Vol. 27, pp. 145-153, Mar. 1989.

- [13] S. J. Whitsitt, "Error estimation and separability measures in feature selection for multiclass pattern recognition," Ph.D. thesis, School Elec. Eng., Purdue Univ., West Lafayette, IN, Aug. 1977.



John P. Kerekes (S'83-M'83) was born in South Bend, IN. He received the B.S.E.E., M.S.E.E., and Ph.D. degrees from Purdue University, West Lafayette, IN, in 1983, 1986, and 1989, respectively.

From 1983 to 1984 he was a member of the technical staff of the Space and Communications Group of the Hughes Aircraft Co., El Segundo, CA, where he performed circuit design for communications satellites. From 1984 to 1989 he was a Graduate Teaching Assistant in the School of Electrical Engineering at Purdue University. From 1986 to 1989 he was a Graduate Research Assistant, working with both the School of Electrical Engineering and the Laboratory for Applications of Remote Sensing. He is presently employed by the Massachusetts Institute of Technology Lincoln Laboratory, Lexington.

Dr. Kerekes is a member of Phi Kappa Phi, Tau Beta Pi, and Eta Kappa Nu.



David A. Landgrebe (S'54-M'57-SM'74-F'77) received the B.S.E.E., M.S.E.E., and Ph.D. degrees from Purdue University, West Lafayette, IN.

He is Professor of Electrical Engineering at Purdue University. His area of speciality in research is communication science and signal processing, especially as applied to Earth observational remote sensing. His research contributions to that field have been in the areas of multispectral pattern recognition, spectral/spatial/temporal classifiers, spectral feature design, and system simulation.

He is also co-author of the text, *Remote Sensing: The Quantitative Approach*, and a contributor to the book, *Remote Sensing of Environment*, and the *ASP Manual of Remote Sensing* (1st ed.). He has been a member of the editorial board of the journal *Remote Sensing of Environment* since its inception, and is also on the editorial board of the journal *Image and Computer Vision*.

Dr. Landgrebe is a member of the American Society of Photogrammetry and Remote Sensing, the American Association for the Advancement of Science and the American Society for Engineering Education. He is also a member of the Eta Kappa Nu, Tau Beta Pi, and Sigma Xi honor societies. He has received both of the outstanding teacher awards given by his department. He has also received the NASA Exceptional Scientific Achievement Medal for his work in the field of machine analysis methods for remotely sensed Earth observational data. He was President of the IEEE Geoscience and Remote Sensing Society during 1986 and 1987 and has been a member of its Administrative Committee since 1979.